Nanoscale Advances

ROYAL SOCIETY OF CHEMISTRY

PAPER

View Article Online
View Journal | View Issue

Check for updates

Cite this: *Nanoscale Adv.*, 2020, **2**, 5688

Rhodium doping augments photocatalytic activity of barium titanate: effect of electronic structure engineering†

D. Krishna Bhat, *[a] Harsha Bantawal[a] and U. Sandhya Shenoy *[b]

Received 23rd August 2020
Accepted 4th November 2020

DOI: 10.1039/d0na00702a

rsc.li/nanoscale-advances

Environmentally friendly $BaTiO_3$ is emerging as a potential photocatalyst due to its tunable electronic structure. Although originally believed to be a poor photocatalyst due to its wide band gap, several strategies have been implemented to reduce its band gap. One such approach is doping, but this often leads to the formation of mid gap recombination centers and diminishes the efficiency of the material. In the present work, we study for the first time the effect of site occupancy of Rh on the electronic structure of $BaTiO_3$. As the theoretical results reveal that if Rh occupies both Ba and Ti sites simultaneously it leads to the formation of mid gap states, an experimental approach is implemented to reduce the band gap of $BaTiO_3$ while simultaneously avoiding the formation of recombination centers. The facile one pot hydrothermal approach reported here directs the Rh towards Ba sites leading to a decrease in the band gap due to the appearance of donor Rh^{3+} states, suppressing the formation of Rh^{4+} states. A promising photocatalytic activity of 96% degradation of methylene blue dye in 120 minutes was observed for the 0.5 Rh sample indicating the high efficiency of the material.

Introduction

The current energy and environmental crises have led to immense interest in the field of photocatalysis, be it hydrogen production *via* water splitting or pollutant degradation by using visible light. Oxides have been the front runners in the field of photocatalysis due to their nontoxic, economical and stable nature.[1,2] Since oxides possess a large band gap which prohibits absorption of the visible range of solar radiation, various strategies such as formation of composites with 2D materials, heterostructures and doping have been implemented to facilitate the process of photocatalysis.[3–6] Among oxides, multi-cation oxides such as tungstates, titanates, and vanadates are a convenient choice as they can provide multiple sites for doping.[7–10] It is well known that $SrTiO_3$, a perovskite material, has been extensively studied for photocatalysis in degradation of methylene blue (MB) dye by tuning its band gap *via* doping, but only a few reports exist on $BaTiO_3$.[11–15]

$BaTiO_3$ is a versatile material with a highly tunable crystal and electronic structure and has the potential of being a multifunctional material.[5,10,16,17] For a material to show enhanced photocatalytic properties it must have a band gap small enough to absorb visible radiation and generate electron–hole pairs, and the photogenerated charge carriers must have sufficient separation to prevent their recombination.[18] So far, the piezoelectric effect of $BaTiO_3$ has been used to enhance the separation of photogenerated charge carriers while it is also combined with some other plasmonic nanomaterials of Ag or Au to further meet the challenge of absorption of visible light radiation.[10,19–21] Besides this, compositing with carbon-based materials has also been adopted to enhance the photocatalytic efficiency *via* promoting charge carrier separation.[14,15,22,23] Various dopants such as Ce, Cr, Fe, In, Mn, Mo, Ni, N, Rh, W, and Zn have been used to reduce the band gap of $BaTiO_3$ and bring its absorption from the UV to the visible region of the solar spectrum, thus improving its photocatalytic efficiency.[4,6,13,17,24–29] Doped $BaTiO_3$ has largely been used for the photocatalytic production of hydrogen rather than degradation of dyes.[4,6,27,30] Doping is well known to largely affect the electronic structure and hence the properties associated with it depending on the site which it occupies.[31,32] Although doping is a promising choice to reduce the band gap, in certain cases it may lead to the formation of acceptor levels leading to the recombination of charge carriers and hence poor efficiency.[12,33] Therefore, we need to keep in mind that in addition to being stable, nontoxic and having an appropriate band gap, the recombination rate should be low with an increase in the lifetime of charge carriers for a material to be an ideal photocatalyst.[18]

Recently, we reported Rh to be an ideal dopant in $SrTiO_3$ for photocatalytic degradation of MB and thermoelectric

[a]*Department of Chemistry, National Institute of Technology Karnataka, Surathkal, Mangalore-575025, India. E-mail: denthajekb@gmail.com*

[b]*Department of Chemistry, College of Engineering and Technology, Srinivas University, Mukka, Mangalore-574146, India. E-mail: sandhyashenoy347@gmail.com*

† Electronic supplementary information (ESI) available. See DOI: 10.1039/d0na00702a

application and found that the site occupancy of the material plays a major role in the performance of the material.[34,35] Although Rh has already been doped in $BaTiO_3$, its efficiency as a photocatalyst has been tested only for hydrogen generation.[36,37] Herein, we theoretically study the effect of Rh on the electronic structure of $BaTiO_3$ and its effect on the band gap of the material. Based on the inputs from the first principles density functional theory (DFT) results, we devised a simple hydrothermal technique which directs Rh towards Ba sites which leads to the formation of donor levels and a decrease in the band gap. We carried out an in-depth analysis of the photocatalytic phenomenon taking place along with thorough characterization of the synthesized material. Since Rh is expensive we tried to make the final material considerably economical by trying to achieve higher efficiency for as low concentration as 0.5 Rh (mol%). 96% degradation was observed in 120 min and the high cycling stability reveals the high efficiency of the material as a photocatalyst in comparison to the 65.2% exhibited by 0.5 Rh doped in $SrTiO_3$.[34]

Methods

Computational details

We simulated the electronic structure of pristine $BaTiO_3$ and Rh-doped $BaTiO_3$ using a $2 \times 2 \times 2$ supercell of primitive $BaTiO_3$. The first principles DFT calculations carried out using the Quantum ESPRESSO package considered the Perdew–Wang (PW) functional type of pseudopotential with local density approximation.[38,39] The norm conserving pseudopotential considered $6s^2$, $3d^24s^2$, $2s^22p^4$, and $4d^85s^1$ of Ba, Ti, O and Rh, respectively, as the valence electrons. The plane wave basis representing the wave functions was terminated with a high energy cutoff and charge density cutoffs of 120 Ry and 480 Ry, respectively. The Brillouin zone was sampled using k point meshes of $4 \times 4 \times 4$ and $8 \times 8 \times 8$ for self-consistent and non-self-consistent field calculations, respectively. The electronic structure was determined along the $\Gamma - X - M - \Gamma - R - X$ high symmetry path.

Synthesis

All the chemicals were purchased from Sigma-Aldrich and were used as received without further purification. 0.35 g of titanium(IV) oxide, anatase (325 mesh powder), was added to 30 mL of 5 M KOH solution. To this, calculated amounts of rhodium(III) chloride and barium hydroxide (octahydrate) were added and stirred for one hour. The resultant mixture was sealed in an autoclave and kept in a hot air oven maintained at 180 °C for 20 hours. The as-obtained precipitates were washed thoroughly with acetic acid and water. The washed products were dried in an oven at 70 °C for 8 hours. The products obtained by using 0.1, 0.3, 0.5, 0.7 and 0.9 mol% of the Rh precursor were labeled 0.1 Rh, 0.3 Rh, 0.5 Rh, 0.7 Rh and 0.9 Rh, respectively.

Characterization

The crystallographic parameters of the synthesized materials were examined by using an X-ray diffractometer (XRD, Rigaku Miniflex 600) equipped with a monochromatic Cu K_α radiation ($\lambda = 0.154$ nm) at a scan rate of 2° min^{-1} in the range of 20–80°. The surface morphological features of the synthesized semiconductors were analyzed using transmission electron microscopy (TEM) and high-resolution transmission electron microscopy (HRTEM, JEOL/JEM 2100). A Kratos XSAM800 spectrometer equipped with an Al K_α source was used to record the X-ray photoelectron spectrum (XPS) to study the surface chemistry and valence states of the material. The specific surface area was determined using the Brunauer–Emmett–Teller (BET) method (BEL SORP II, JAPAN). The pore size distribution was determined using the Barrett–Joyner–Halenda (BJH) method. The diffuse reflectance (DR) spectra were recorded using a UV-visible spectrometer (DRS, DR SPECORD S600 Analytic Jena). The photoluminescence (PL) spectra were recorded at room temperature (LS-55, PerkinElmer).

Determination of photocatalytic activity

A photocatalytic reactor provided with a high-pressure 250 W Hg vapor lamp (used as a visible light source) was used for the photocatalytic degradation measurements. Before photocatalytic studies, the photocatalyst (50 mg) was dispersed in 50 mL of MB solution (10 mg L^{-1}) with the help of a sonicator for 5 minutes. The resultant solution was loaded into the reactor and then the visible light source was turned on. 5 mL of the solution was withdrawn periodically, centrifuged in order to separate the catalyst and the absorbance of the supernatant dye solution was measured using a UV-visible spectrometer at 664 nm. The percentage degradation of dye was calculated as per eqn (1).

$$\text{Degradation}\% = [(C_o - C)/C_o] \times 100 \quad (1)$$

where C_o is the initial concentration of the solution and C is the concentration at different intervals of time.[1,7]

Results and discussion

Electronic structure analysis

$BaTiO_3$, a perovskite material, has a cubic structure formed out of Ba atoms occupying the corner, a Ti atom occupying the center and O atoms occupying the 6 face centers.[16] It is well known that in the electronic structure of the primitive $BaTiO_3$ there exists a direct band gap at the Γ point while two indirect gaps appear from $R \rightarrow \Gamma$ and $M \rightarrow \Gamma$. In the electronic structure of the $2 \times 2 \times 2$ supercell of $BaTiO_3$ we observe that a direct band gap of 1.929 eV appears at the Γ point (Fig. 1a). This is due to the folding of the R point of the primitive cell onto the Γ point of the $2 \times 2 \times 2$ supercell.[16] Hence, the indirect band gap between Γ and R points appears as a direct band gap at the Γ point. The original direct band gap at the Γ point of the primitive cell appears as the distance between the conduction band minimum and the second set of bands beneath the valence band maximum at the Γ point, measuring 2.304 eV.[16] The band which exists between this and the valence band maximum is formed due to the overlapping of the M point of the primitive cell onto the Γ point of the supercell and measures 1.994 eV.[16]

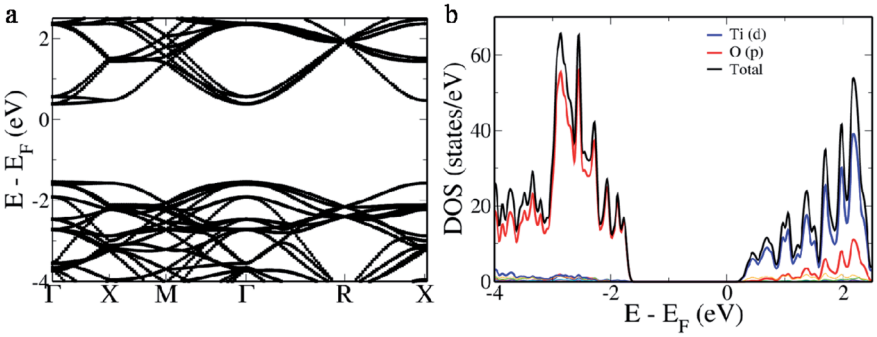

Fig. 1 (a) Electronic structure and (b) pDOS of the 2 × 2 × 2 supercell of $BaTiO_3$.

The band gap is typically underestimated in DFT based calculations due to the presence of discontinuities in the derivative of energy.[40] To understand the contributions from various atomic orbitals, we projected them onto the density of states (DOS). We see that the O 'p' orbitals form the valence band, while the Ti 'd' orbitals form the conduction band (Fig. 1b). Conduction bands also reveal the presence of contributions from O 'p' orbitals. As Ba atoms have ionic nature, we do not see their contributions in the pDOS plot.[16]

Since there is a possibility of Rh atoms occupying both the sites simultaneously (case A) or either Ti sites (case B) or Ba sites (case C) only, we simulated the electronic structure for all three conditions. When Rh atoms occupy one Ba site and one Ti site (case A), we see that the electronic structure reveals the occurrence of an acceptor level within the band gap with a width of 0.167 eV above the Fermi level, effectively decreasing the material band gap to 0.673 eV (Fig. 2a). The lifetime of the photogenerated electrons and holes is largely affected due to the presence of this acceptor level as it can act as a recombination center. On careful observation of pDOS, we find that the acceptor level is formed due to the hybridization of 'd' orbitals of Rh atoms in Ba sites and 'p' orbitals of O atoms (Fig. 2b). However, the valence band edge is formed out of contribution from 'd' orbitals of both the Rh atoms along with 'p' orbitals of the O atoms. We see a large gap of 1.032 eV between the edge of the valence band and the acceptor level which effectively prevents the replenishment of electrons leading to a larger lifetime of the recombination center.[34]

We further visualized the wavefunctions at the Γ point at various energy levels marked in the pDOS plot given in Fig. S1.† Hyper deep defect states appear at region I due to the 'd' states of Rh atoms (Fig. 3a).[41] While we observe the contributions of 'p' orbitals of O in the valence band regions II and III, contributions of 'd' orbitals of both the Rh atoms were also dominant at the valence band edge (Fig. 3b and c). In region IV we clearly see the contribution due to 'd' orbitals of Rh in the Ba site while minor contribution from 'd' orbitals of Rh in the Ti site is seen at the conduction band edge in region V along with major contributions from 'd' orbitals of Ti (Fig. 3d and e). Upper conduction bands in region VI show major contributions from 'd' orbitals of Ti and 'p' orbitals of O atoms (Fig. 3f).

In case B, we estimate a direct band gap of 2.028 eV at the Γ point and an indirect band gap of 1.796 eV from $X \rightarrow G$. The indirect band gap is a consequence of overlapping of the defect band with the valence band edge (Fig. 4a). pDOS reveals this area of overlap as hybridization of 'p' orbitals of O with 'd' orbitals of Rh while rest of the contributions remain the same as that of the pristine $BaTiO_3$ (Fig. 4b). In case C, we observe in the electronic structure, a separate donor level having a width of 0.363 eV formed 0.148 eV above the valence band edge (Fig. 5a). This effectively reduces the band gap to 1.525 eV making it the lowest value in all three cases. The pDOS reveals that while the valence band is formed out of major contribution of 'p' orbitals

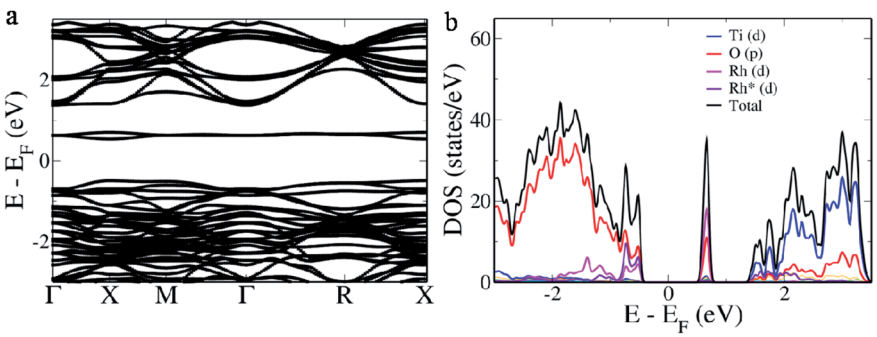

Fig. 2 (a) Electronic structure and (b) pDOS of the 2 × 2 × 2 supercell of Rh-doped $BaTiO_3$ (case A) with one Rh in the Ti site (lavender) indicated as Rh* and another Rh in the Ba site (pink).

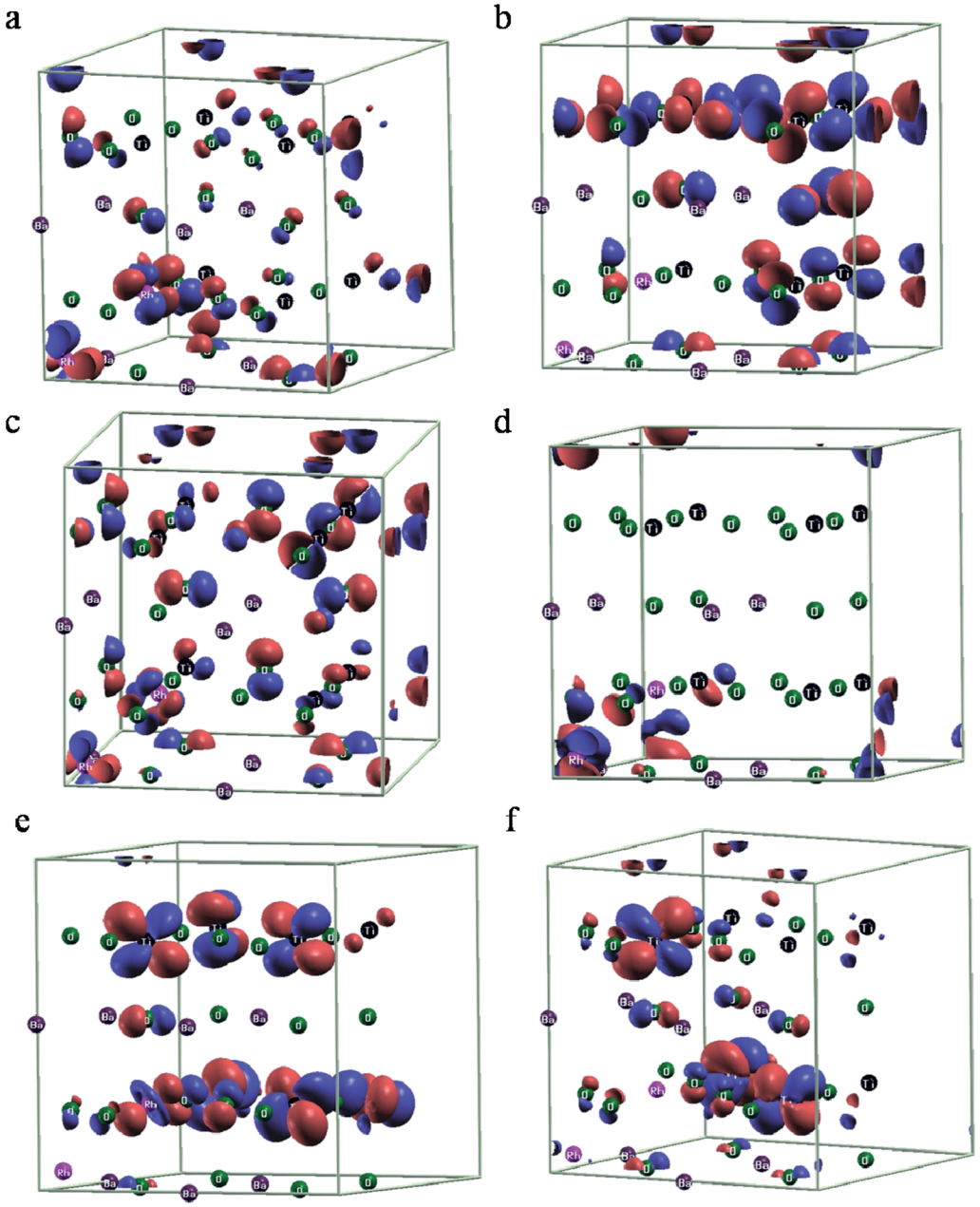

Fig. 3 Wavefunction visualization at the Γ point (a–f) corresponding to various energy levels as indicated by Roman numerals I–VI in the pDOS in Fig. S1,† respectively, for case A. Red and blue colors indicate the positive and negative lobes of the orbitals.

of O, it also hybridizes with 'd' orbitals of Rh to form the donor level and shows minor contributions in the conduction band which has major contributions from 'd' orbitals of the Ti atom (Fig. 5b). For easy migration of photogenerated charge carriers, continuous nature of the band is essential which is seen in the case of single occupancy.[34]

Further, we increased the concentration of Rh in $BaTiO_3$ by substituting two Rh in Ba sites. In the electronic structure, we see that with the increase in the concentration of Rh the width of the donor level increases to 0.472 eV. Also, it revealed a further decrease in the band gap to 1.461 eV predicting better absorption of visible light and hence higher photocatalytic efficiency consistent with the experiments (Fig. S2†). It is seen that when Rh occupies the Ba site, the band gap decreases to a maximum extent indicating the extension of light absorption to the visible region. Also, since the donor level is only slightly above the valence band within the Fermi level, rapid replenishment of electrons would occur avoiding the formation of trap centers, thus increasing the carrier life time.[34,42] The results from the DFT calculations reveal that a synthetic method to direct Rh towards the Ba site would help in developing a better photocatalyst than Rh in the Ti site. Furthermore, if Rh occupies both the sites then the material would not be an ideal photocatalyst. Hence, we

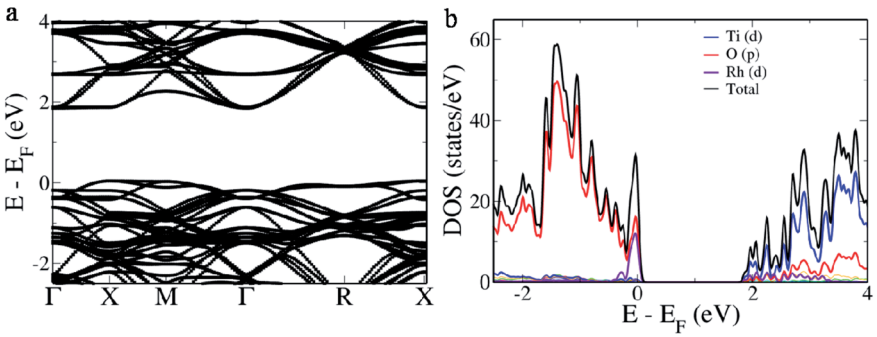

Fig. 4 (a) Electronic structure and (b) pDOS of the 2 × 2 × 2 supercell of Rh-doped $BaTiO_3$ (case B) with Rh in the Ti site.

adopted a hydrothermal approach to direct Rh towards the Ba site during the synthesis so that a photocatalyst with reduced band gap and donor levels is formed without creation of the recombination centers.

XRD analysis

We observe that the XRD pattern of the synthesized samples matched well with the cubic phase of $BaTiO_3$ (JCPDS card no. 00-031-0174) indicating that both doped and undoped samples had the same crystal structure (Fig. 6). We were not able to see any impurity peaks, which indicated the high purity of the synthesized samples. The ionic radii of Rh^{3+}, Ba^{2+} and Ti^{4+} are 0.067 nm, 0.161 nm and 0.061 nm, respectively, which means that Rh should preferably be doped in the Ti site. Substitution in the Ti site would have caused a slight increase in the lattice parameter which was not the case here. The synthetic approach we adopted directs the Rh towards the Ba site which leads to a reduction in the lattice parameter to 4.02 Å. This manifests as shifting of peaks towards higher θ values in the doped samples with respect to the undoped $BaTiO_3$ (Fig. S3†).

XPS analysis

The XPS survey spectrum indicated the presence of Ba, Ti, O and Rh species in the sample (Fig. S4†). We observe that Ba 3d has two spin states Ba $3d_{5/2}$ and Ba $3d_{3/2}$ which appear at binding energies of 778.74 eV and 794.03 eV, respectively, as peaks (Fig. 7a). The binding energy separation of 15.29 eV between the two spin states of Ba confirmed the oxidation state of Ba in $BaTiO_3$ as +2.[7,43] The high-resolution spectrum of Ti indicates that it is in the +4 oxidation state as peaks emerge at binding energies of 458.42 eV (for Ti $2p_{3/2}$) and 464.19 eV (for Ti $2p_{1/2}$), respectively (Fig. 7b).[3] Further, the peaks at binding energies 529.61 eV and 531.45 eV can be attributed to the lattice oxygen (O_L) and surface hydroxyl groups (O_{OH}), respectively (Fig. 7c).[44,45] The deconvoluted peaks of Rh at binding energies 310.10 eV and 314.58 eV can be allotted to the Rh $3d_{5/2}$ and Rh $3d_{3/2}$ spin states, respectively (Fig. 7d). These binding energy values

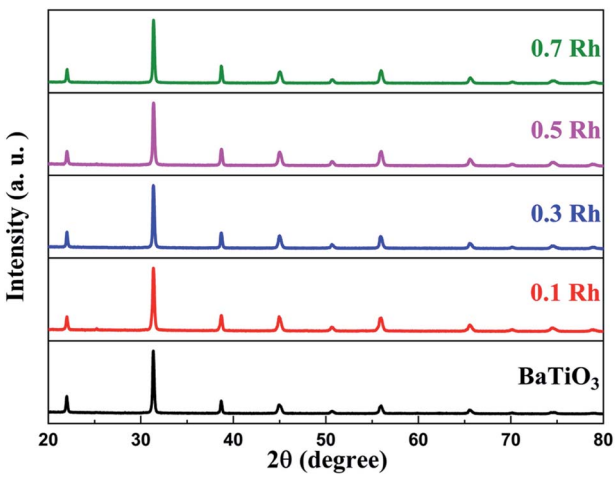

Fig. 6 XRD patterns of $BaTiO_3$ and Rh-doped $BaTiO_3$ with varying concentrations of Rh.

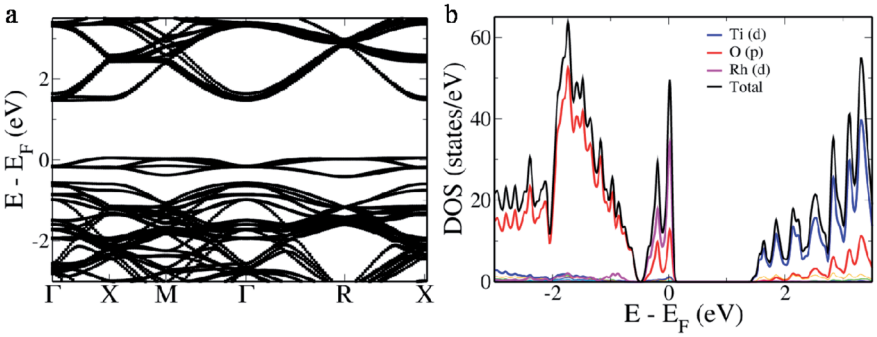

Fig. 5 (a) Electronic structure and (b) of the 2 × 2 × 2 supercell of Rh-doped $BaTiO_3$ (case C) with Rh in the Ba site.

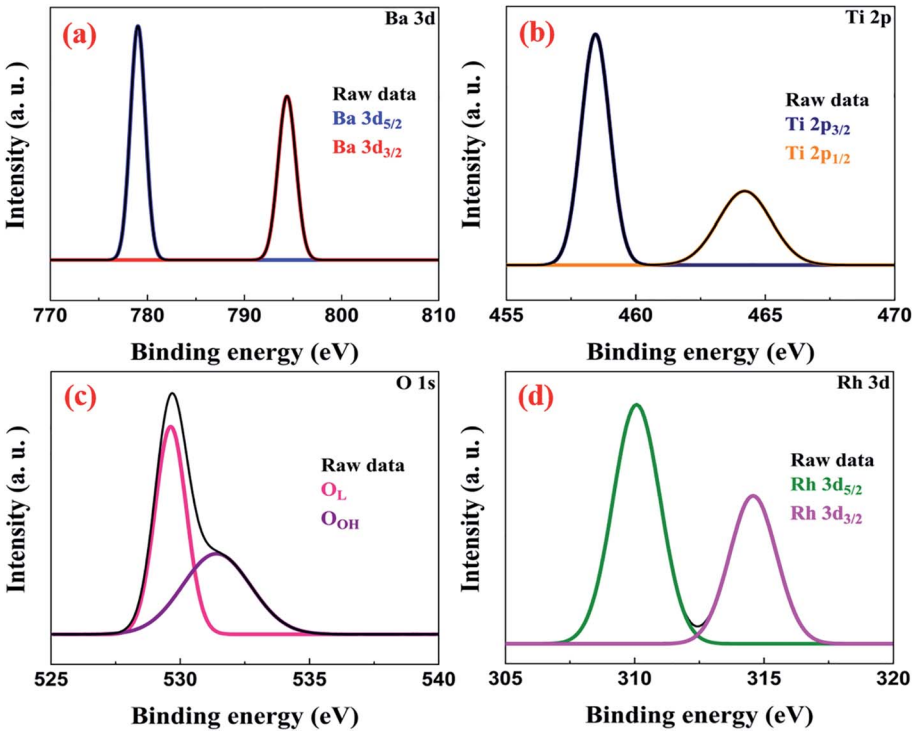

Fig. 7 High-resolution XPS plot of (a) Ba 3d, (b) Ti 3p, (c) O 1s and (d) Rh 3d.

indicated the successful incorporation of Rh^{3+} ions into the lattice of $BaTiO_3$ and not Rh^{4+}.[34,36]

Morphology and surface area analysis

We studied the morphology of the samples using TEM. We observe that undoped $BaTiO_3$ has a cubooctahedral shape, while doping it with Rh makes it cubic in structure (Fig. 8a and b). We observe the 110 planes in the HRTEM image of the 0.5 Rh sample with a spacing of 0.28 nm (Fig. 8c). The single crystalline nature of the synthesized 0.5 Rh sample indicates the success of the employed synthetic technique. The elemental composition studied using EDX reveals Ba, Ti, O and Rh as the elements present, confirming the results from XPS (Fig. 8d). The spot EDX confirms the uniform distribution of the atoms in the sample (Fig. S5†).

Since the surface area of the sample plays a huge role in the catalysis process, we studied the surface area of both doped and undoped $BaTiO_3$. In the nitrogen adsorption–desorption isotherms of $BaTiO_3$ and 0.5 Rh samples we observe a type IV pattern with hysteresis loops being type H3, indicating the presence of slit like pores (Fig. S6 and S9†).[46] The BET surface area was found to be 7 $m^2\ g^{-1}$ for the 0.5 Rh sample, which is higher than that of pure $BaTiO_3$ (4.5 $m^2\ g^{-1}$). This higher surface area of the 0.5 Rh sample will be highly beneficial for the effective adsorption and degradation of the pollutants. A broad BJH pore size distribution in the range of 2–100 nm indicated the presence of mesopores and macropores (inset of Fig. 9).[47] The pore volume of the 0.5 Rh sample was found to be 0.0419 $cm^3\ g^{-1}$ which is almost twice that of the pristine sample (0.0229 $cm^3\ g^{-1}$), which helps in the efficient photo-absorption and diffusion of molecules during the photo-catalytic reaction.

Optical absorbance analysis

In the DR spectra of pristine $BaTiO_3$ we observe an absorption edge at around 400 nm due to the electronic transitions from the O 'p' orbitals to the Ti 'd' orbitals (Fig. 10a). However, the absorption edges of Rh-doped samples are red shifted to the visible region (400–550 nm) due to the decrease in the band gap. These wavelengths can be attributed to the electronic transitions from the donor level formed by the Rh^{3+} species to the conduction band of $BaTiO_3$. The characteristic absorption peak at 580 nm, caused by Rh^{4+}, was absent indicating that Rh was doped in the +3 oxidation state further confirming the results from XPS.[34,48]

The direct band gap of the samples was calculated using the Tauc relation using eqn (2).

$$(\alpha h\nu)^2 = K(h\nu - E_g) \quad (2)$$

Where α is the absorption coefficient, E_g is the band gap energy of the semiconductor, K is a constant, and $h\nu$ is the photon energy. The band gap energies of $BaTiO_3$, 0.1 Rh, 0.3 Rh, 0.5 Rh and 0.7 Rh samples estimated from their respective absorption edge values were found to be 3.04 eV, 2.37 eV, 2.34 eV, 2.26 eV and 2.17 eV, respectively. We observe a red shift in the absorption peak accompanied by a decrease in the band gap with an increase in the concentration of Rh doping due to the

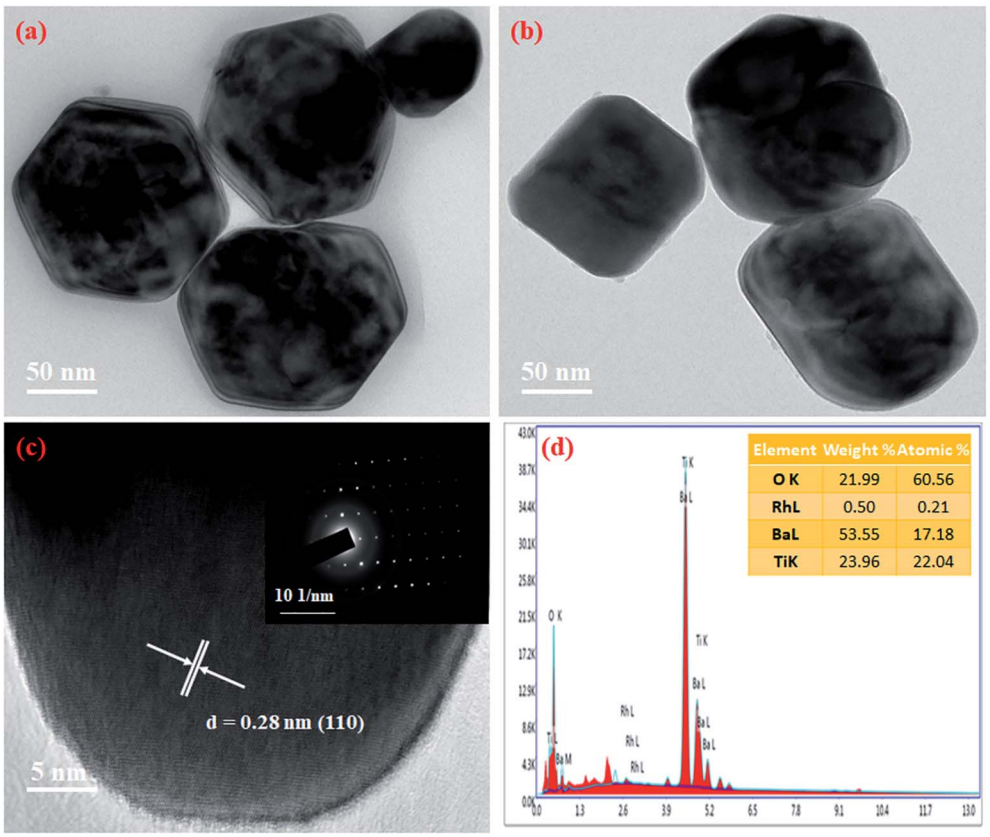

Fig. 8 (a) TEM image of $BaTiO_3$, (b) TEM image of 0.5 Rh, (c) HRTEM of 0.5 Rh (inset shows the SAED pattern of the 0.5 Rh sample) and (d) EDX spectrum of 0.5 Rh samples.

increase in the width of the donor level which further gets closer to the conduction band.

In the PL spectra of $BaTiO_3$ and Rh-doped $BaTiO_3$, we can observe that there is a noticeable drop in the fluorescence intensity for the doped samples compared to that of the pristine sample, which indicates the lower opportunity for the recombination of photoinduced charges in the case of doped samples (Fig. 10b).[49] The electrons are rapidly replenished to the vacant site by the valence band as discussed in the DFT results which prevents their recombination with the holes generated. Thus, more photoinduced holes and electrons can participate in the photocatalytic reactions. It can be noted that the PL intensity decreases till 0.5 Rh and beyond this concentration the PL intensity increases which can be attributed to the formation of recombination centers probably due to mixed occupancies as revealed by DFT studies.

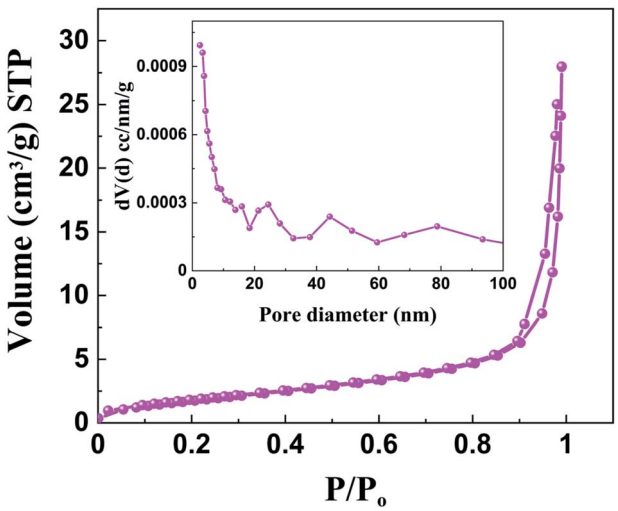

Fig. 9 BET surface area analysis of the 0.5 Rh sample (inset shows the pore size distribution).

Photocatalytic activity

The photocatalytic efficiency of the synthesized materials was evaluated for the decomposition of MB dye under irradiation of visible light. Fig. 11a shows the photocatalytic degradation curves of MB in the presence of $BaTiO_3$ and Rh-doped $BaTiO_3$ samples. The percentage degradation of MB by $BaTiO_3$, 0.1 Rh, 0.3 Rh, 0.5 Rh and 0.7 Rh samples was found to be 45, 55, 69, 96 and 73, respectively. We observed that the photocatalytic activity of Rh-doped samples was higher than that of the pristine sample, which could be attributed to the formation of Rh^{3+} donor levels above the valence band which efficiently decreased the band gap enabling harvesting of the visible light. The 0.5 Rh sample exhibited the highest photocatalytic activity beyond

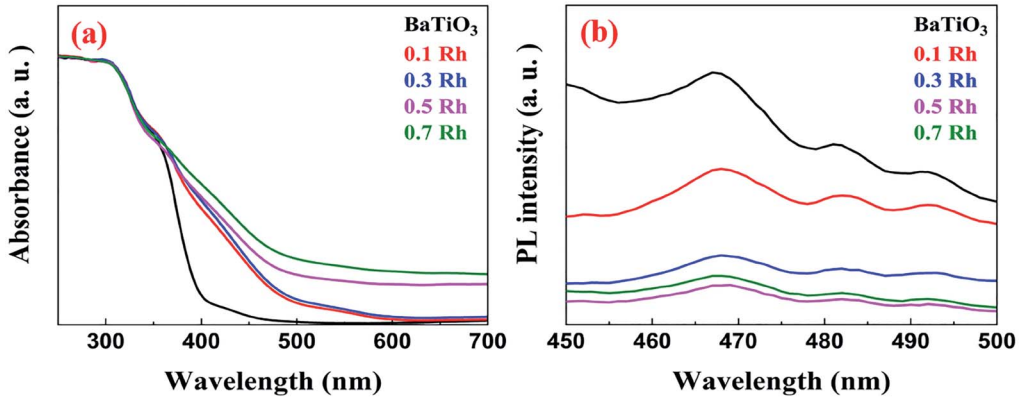

Fig. 10 (a) DR and (b) PL spectra of $BaTiO_3$ and Rh-doped $BaTiO_3$ samples.

which the activity decreased. This is due to the fact that even though the doping of Rh decreased the band gap, at higher concentration there is larger scope for mixed occupancy leading to the formation of recombination centers as revealed by the DFT calculations. This fact is also supported by the PL studies above. To further confirm this fact, we synthesized the 0.9 Rh sample and tested its photocatalytic activity. The characterization results and the photocatalytic activity are provided in Fig. S7.† We observe that the 0.9 Rh sample shows the least activity of 57% with a rate constant of 0.0068 min^{-1}.

The kinetics of the photocatalytic degradation of MB by $BaTiO_3$ and Rh-doped $BaTiO_3$ samples are well in agreement with the pseudo first-order rate equation given by eqn (3).

$$\ln(C/C_o) = -kt \quad (3)$$

where C_o is the initial concentration of the dye, C is the concentration of the dye at time 't' and k is the first order rate constant, which was calculated from the slope of the straight line obtained by plotting $-\ln(C/C_o)$ *versus* 't'.[49] The rate constant of the 0.5 Rh sample was found to be higher than that of all the synthesized samples (Fig. 11b). Further, the 0.5 Rh sample showed only a marginal drop in the photocatalytic efficiency even after five consecutive cycles, suggesting its high stability and reusability towards photocatalytic degradation reactions (Fig. S8†). Comparison of the photocatalytic activity of this material with that of the previously reported ones shows that the 0.5 Rh sample is highly efficient (Table S1†).

The thermodynamic parameters such as energy of activation (E_a), free energy of activation ($\Delta G^{\#}$), enthalpy of activation ($\Delta H^{\#}$) and entropy of activation ($\Delta S^{\#}$) were computed by employing activation complex theory (ACT) and Eyring equation as described in the previous reports.[12] We see from Table 1 that the photodegradation of MB without a catalyst requires higher energy of activation while by using $BaTiO_3$ and Rh-doped $BaTiO_3$ catalysts, relatively lower energy of activation is needed, with the 0.5 Rh sample having the least value. This

Table 1 Thermodynamic parameters of $BaTiO_3$ and Rh-doped $BaTiO_3$ samples

Sample	E_a (kJ mol^{-1})	$\Delta H^{\#}$ (kJ mol^{-1})	$\Delta S^{\#}$ (kJ mol^{-1})	$\Delta G^{\#}$ (kJ mol^{-1})
Without catalyst	17.7	15.2	−0.25	91.2
$BaTiO_3$	13.2	10.7	−0.25	86.6
0.1 Rh	12.5	10.0	−0.25	85.9
0.3 Rh	11.6	9.1	−0.25	85.0
0.5 Rh	9.3	6.8	−0.25	82.7
0.7 Rh	11.3	8.8	−0.25	84.7
0.9 Rh	12.4	9.9	−0.25	85.8

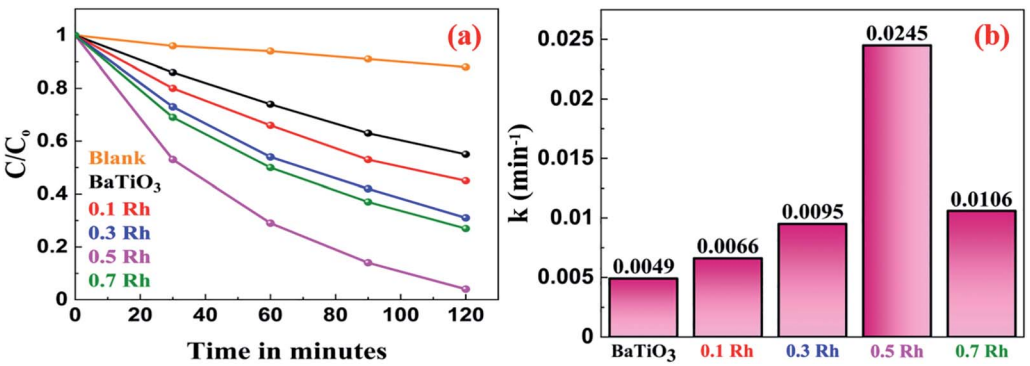

Fig. 11 (a) The photocatalytic degradation of MB and (b) the rate constants of the photocatalytic degradation of MB by the synthesized $BaTiO_3$ and Rh-doped $BaTiO_3$.

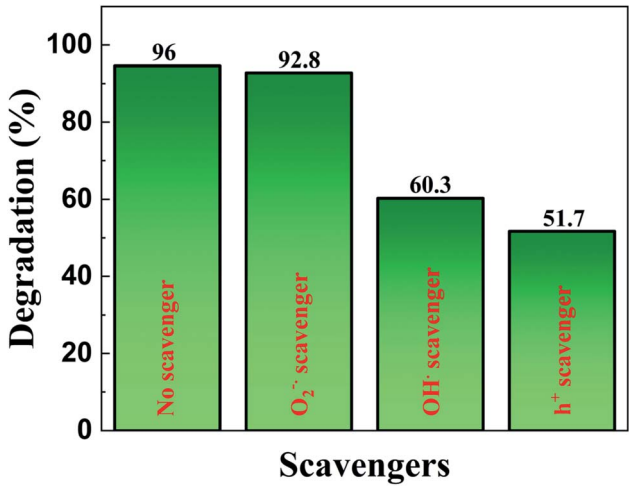

Fig. 12 Effect of radical scavengers on the photocatalytic degradation of MB by the 0.5 Rh sample.

indicates that addition of catalysts alters the reaction pathway, which confirms that the catalyst alters the path of the reaction by lowering the activation energy. Positive enthalpy and free energy change indicate that the reaction is endothermic and not spontaneous.

We also carried out trapping experiments in order to assess the active species involved in the photocatalytic degradation by following the same procedure as that of photocatalytic activity evaluation but with the aid of different radical scavenging agents such as benzoquinone (1 mM) as a superoxide anion radical ($O_2^{\cdot-}$) scavenger, potassium iodide (10 mM) as a hole (h^+) scavenger and isopropyl alcohol (10 mM) as a hydroxyl radical ($OH^{\cdot}$) scavenger. In Fig. 12 we observe that superoxide radical anions are not the major active species as the corresponding scavenger benzoquinone did not deteriorate the photocatalytic activity to a larger extent. However, the addition of potassium iodide and isopropyl alcohol reduced the photocatalytic activity significantly. As a result, holes followed by hydroxyl radicals are considered to be the active species for the effectual degradation of the dye.

Based on the above study we propose a mechanism for the photocatalytic degradation of MB dye as follows: when the 0.5 Rh sample gets irradiated with an energy greater than or equal to its band gap, the electrons from the donor levels formed by Rh^{3+} species are transferred to the conduction band. Later, these electrons react with oxygen to produce superoxide anion radicals. The formed holes either directly react with MB to produce degradation products or react with surface hydroxyl groups to produce hydroxyl radicals. The formed superoxide and hydroxyl radicals react with dye molecules to produce harmless degradation products (Fig. 13).

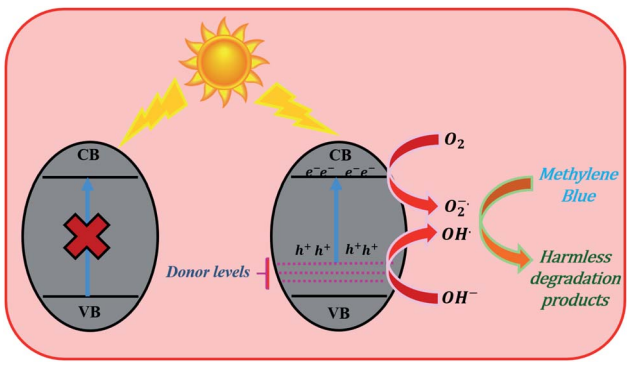

Fig. 13 The photocatalytic mechanism of Rh-doped $BaTiO_3$ for the degradation of MB under visible light irradiation.

Conclusions

Herein, we report a facile synthesis of Rh-doped $BaTiO_3$ and its study as a photocatalyst in the degradation of MB. The experimental approach was designed by making use of first principles DFT calculations. The theoretical study revealed that by directing Rh towards either the Ba site or Ti site, only donor levels would be formed leading to a decreased band gap while simultaneous occupation of Ba and Ti sites would lead to the formation of acceptor states detrimental to the photocatalytic activity. Based on the above, we adopted a hydrothermal approach to direct Rh towards the Ba site. This led to the decrease in the band gap and extension of absorption to the visible region of the spectrum. The absence of recombination centers in 0.5 Rh samples led to increased photocatalytic activity with 96% MB degradation in 2 h revealing the approach to be successful even at low concentrations of Rh. This approach can very well be extended to other perovskite oxides to improve their efficiency in photocatalytic degradation of dyes.

Conflicts of interest

There are no conflicts to declare.

References

1 M. M. J. Sadiq, U. S. Shenoy and D. K. Bhat, $NiWO_4$-ZnO-NRGO Ternary Nanocomposite as an Efficient Photocatalyst for Degradation of Methylene Blue and Reduction of 4-Nitro Phenol, *J. Phys. Chem. Solids*, 2017, **109**, 124–133.

2 S. Kampouri and K. C. Stylianou, Dual-Functional Photocatalysis for Simultaneous Hydrogen Production and Oxidation of Organic Substances, *ACS Catal.*, 2019, **9**, 4247–4270.

3 H. Bantawal, M. Sethi, U. S. Shenoy and D. K. Bhat, Porous Graphene Wrapped $SrTiO_3$ Nanocomposite: Sr–C Bond as an Effective Coadjutant for High Performance Photocatalytic Degradation of Methylene Blue, *ACS Appl. Nano Mater.*, 2019, **2**, 6629–6636.

4 D. Zhong, W. Liu, P. Tan, A. Zhu, L. Qiao, Y. Bian and J. Pan, Efficient Hydrogen Generation of Indium Doped $BaTiO_3$ Decorated with CdSe Quantum Dots: Novel Understanding of the Effect of Doping Strategy, *Int. J. Hydrogen Energy*, 2019, **44**, 1627–1639.

5 A. Ali, Y. Liang, S. Ahmed, B. Yang, B. Guo and Y. Yang, Mutual Contaminants Relational Realization and

Photocatalytic Treatment Using Cu_2MgSnS_4 Decorated $BaTiO_3$, *Applied Materials Today*, 2020, **18**, 100534.

6 J. P. Zou, L. Z. Zhang, S. L. Luo, L. H. Leng, X. B. Luo, M. J. Zhang, Y. Luo and G. C. Guo, Preparation and Photocatalytic Activities of Two New Zn-Doped $SrTiO_3$ and $BaTiO_3$ Photocatalysts for Hydrogen Production from Water without Cocatalysts Loading, *Int. J. Hydrogen Energy*, 2012, **37**, 17068–17077.

7 M. M. J. Sadiq, U. S. Shenoy and D. K. Bhat, Synthesis of $BaWO_4$/NRGO–gC_3N_4 Nanocomposites with Excellent Multifunctional Catalytic Performance via Microwave Approach, *Frontiers of Materials Science*, 2018, **12**, 247–263.

8 M. M. J. Sadiq, U. S. Shenoy and D. K. Bhat, Enhanced Photocatalytic Performance of N-Doped RGO-$FeWO_4$/Fe_3O_4 Ternary Nanocomposite in Environmental Applications. *Mater*, *Today Chem.*, 2017, **4**, 133–141.

9 X. Huang, G. Zhao, G. Wang and J. T. Irvine, Synthesis and Applications of Nanoporous Perovskite Metal Oxides, *Chem. Sci.*, 2018, **9**, 3623–3637.

10 S. Xu, L. Guo, Q. Sun and Z. L. Wang, Piezotronic Effect Enhanced Plasmonic Photocatalysis by AuNPs/$BaTiO_3$ Heterostructures, *Adv. Funct. Mater.*, 2019, **29**, 1808737.

11 H. Bantawal, U. S. Shenoy and D. K. Bhat, Tuning the Photocatalytic Activity of $SrTiO_3$ by Varying the Sr/Ti Ratio: Unusual Effect of Viscosity of the Synthesis Medium, *J. Phys. Chem. C*, 2018, **122**, 20027–20033.

12 H. Bantawal, U. S. Shenoy and D. K. Bhat, Vanadium-Doped $SrTiO_3$ Nanocubes: Insight into Role of Vanadium in Improving the Photocatalytic Activity, *Appl. Surf. Sci.*, 2020, **513**, 145858.

13 M. Nageri and V. Kumar, Manganese-Doped $BaTiO_3$ Nanotube Arrays for Enhanced Visible Light Photocatalytic Applications, *Mater. Chem. Phys.*, 2018, **213**, 400–405.

14 Z. Mengting, T. A. Kurniawan, S. Fei, T. Ouyang, M. H. D. Othman, M. Rezakazemi and S. Shirazian, Applicability of $BaTiO_3$/Graphene Oxide (GO) Composite for Enhanced Photodegradation of Methylene Blue (MB) in Synthetic Wastewater under UV–Vis Irradiation, *Environ. Pollut.*, 2019, **255**, 113182.

15 R. X. Wang, Q. Zhu, W. S. Wang, C. M. Fan and A. W. Xu, $BaTiO_3$–Graphene Nanocomposites: Synthesis and Visible Light Photocatalytic Activity, *New J. Chem.*, 2015, **39**, 4407–4413.

16 U. S. Shenoy and D. K. Bhat, Vanadium Doped $BaTiO_3$ as High Performance Thermoelectric Material: Role of Electronic Structure Engineering, *Mater. Today Chem.*, 2020, **18**, 100384.

17 H. Xiao, C. Luo, G. Huangfu and Y. Guo, Boosting the Photocatalytic Ability of Bandgap Engineered $(Na_{0.5}Bi_{0.5})TiO_3$-$BaTiO_3$ by N-Ni Codoping, *J. Phys. Chem. C*, 2020, **124**, 11810–11818.

18 M. J. S. Mohamed, S. Shenoy and D. K. Bhat, Novel NRGO-$CoWO_4$-Fe_2O_3 Nanocomposite as an Efficient Catalyst for Dye Degradation and Reduction of 4-Nitrophenol, *Mater. Chem. Phys.*, 2018, **208**, 112–122.

19 D. Liu, C. Jin, F. Shan, J. He and F. Wang, Synthesizing $BaTiO_3$ Nanostructures to Explore Morphological Influence, Kinetics, and Mechanism of Piezocatalytic Dye Degradation, *ACS Appl. Mater. Interfaces*, 2020, **12**, 17443–17451.

20 X. Liu, L. Xiao, Y. Zhang and H. Sun, Significantly Enhanced Piezo-Photocatalytic Capability in $BaTiO_3$ Nanowires for Degrading Organic Dye, *Journal of Materiomics*, 2020, **6**, 256–262.

21 S. Xu, Z. Liu, M. Zhang and L. Guo, Piezotronics Enhanced Photocatalytic Activities of Ag-$BaTiO_3$ Plasmonic Photocatalysts, *J. Alloys Compd.*, 2019, **801**, 483–488.

22 T. Xian, H. Yang, L. J. Di and J. F. Dai, Enhanced Photocatalytic Activity of $BaTiO_3$@ g-C_3N_4 for the Degradation of Methyl Orange under Simulated Sunlight Irradiation, *J. Alloys Compd.*, 2015, **622**, 1098–1104.

23 P. Demircivi, B. Gulen, E. B. Simsek and D. Berek, Enhanced Photocatalytic Degradation of Tetracycline using Hydrothermally Synthesized Carbon Fiber Decorated $BaTiO_3$, *Mater. Chem. Phys.*, 2020, **241**, 122236.

24 P. Senthilkumar, D. A. Jency, T. Kavinkumar, D. Dhayanithi, S. Dhanuskodi, M. Umadevi, S. Manivannan, N. V. Giridharan, V. Thiagarajan, M. Sriramkumar and K. Jothivenkatachalam, Built-in Electric Field Assisted Photocatalytic Dye Degradation and Photoelectrochemical Water Splitting of Ferroelectric Ce Doped $BaTiO_3$ Nanoassemblies, *ACS Sustainable Chem. Eng.*, 2019, **7**, 12032–12043.

25 I. C. Amaechi, G. Kolhatkar, A. H. Youssef, D. Rawach, S. Sun and A. Ruediger, B-Site Modified Photoferroic Cr^{3+}-Doped Barium Titanate Nanoparticles: Microwave-Assisted Hydrothermal Synthesis, Photocatalytic and Electrochemical Properties, *RSC Adv.*, 2019, **9**, 20806–20817.

26 I. C. Amaechi, A. H. Youssef, G. Kolhatkar, D. Rawach, C. Gomez-Yañez, J. P. Claverie, S. Sun and A. Ruediger, Ultrafast Microwave-Assisted Hydrothermal Synthesis and Photocatalytic Behaviour of Ferroelectric Fe^{3+}-Doped $BaTiO_3$ Nanoparticles under Simulated Sunlight, *Catal. Today*, 2019, DOI: 10.1016/j.cattod.2019.07.021.

27 P. Xie, F. Yang, R. Li, C. Ai, C. Lin and S. Lin, Improving Hydrogen Evolution Activity of Perovskite $BaTiO_3$ with Mo Doping: Experiments and First-Principles Analysis, *Int. J. Hydrogen Energy*, 2019, **44**, 11695–11704.

28 J. Cao, Y. Ji, C. Tian and Z. Yi, Synthesis and Enhancement of Visible Light Activities of Nitrogen-Doped $BaTiO_3$, *J. Alloys Compd.*, 2014, **615**, 243–248.

29 P. Demircivi and E. B. Simsek, Visible-Light-Enhanced Photoactivity of Perovskite-Type W-Doped $BaTiO_3$ Photocatalyst for Photodegradation of Tetracycline, *J. Alloys Compd.*, 2019, **774**, 795–802.

30 H. C. Huang, C. L. Yang, M. S. Wang and X. G. Ma, Chalcogens Doped $BaTiO_3$ for Visible Light Photocatalytic Hydrogen Production from Water Splitting, *Spectrochim. Acta, Part A*, 2019, **208**, 65–72.

31 S. Shenoy and D. K. Bhat, Enhanced Bulk Thermoelectric Performance of $Pb_{0.6}Sn_{0.4}Te$: Effect of Magnesium Doping, *J. Phys. Chem. C*, 2017, **121**, 20696–20703.

32 U. S. Shenoy and D. K. Bhat, Enhanced Thermoelectric Properties of Vanadium Doped $SrTiO_3$: A Resonant Dopant Approach, *J. Alloys Compd.*, 2020, **832**, 154958.
33 T. Hisatomi and K. Domen, Reaction Systems for Solar Hydrogen Production via Water Splitting with Particulate Semiconductor Photocatalysts, *Nat. Catal.*, 2019, **2**, 387–399.
34 U. S. Shenoy, H. Bantawal and D. K. Bhat, Band Engineering of $SrTiO_3$: Effect of Synthetic Technique and Site Occupancy of Doped Rhodium, *J. Phys. Chem. C*, 2018, **122**, 27567–27574.
35 U. S. Shenoy and D. K. Bhat, Electronic Structure Engineering of $SrTiO_3$ via Rhodium doping: A DFT Study, *J. Phys. Chem. Solids*, 2021, **148**, 109708.
36 K. Maeda, Rhodium-Doped Barium Titanate Perovskite as a Stable p-Type Semiconductor Photocatalyst for Hydrogen Evolution under Visible Light, *ACS Appl. Mater. Interfaces*, 2014, **6**, 2167–2173.
37 S. Nishioka and K. Maeda, Hydrothermal Synthesis of Rhodium-Doped Barium Titanate Nanocrystals for Enhanced Photocatalytic Hydrogen Evolution under Visible Light, *RSC Adv.*, 2015, **5**, 100123–100128.
38 P. Giannozzi, S. Baroni, N. Bonini, M. Calandra, R. Car, C. Cavazzoni, D. Ceresoli, G. L. Chiarotti, M. Cococcioni, I. Dabo, A. L. Corso, S. de Gironcoli, S. Fabris, G. Fratesi, R. Gebauer, U. Gerstmann, C. Gougoussis, A. Kokalj, M. Lazzeri, L. Martin-Samos, N. Marzari, F. Mauri, R. Mazzarello, S. Paolini, A. Pasquarello, L. Paulatto, C. Sbraccia, S. Scandolo, G. Sclauzero, A. P. Seitsonen, A. Smogunov, P. Umari and R. M. Wentzcovitch, Quantum ESPRESSO: A Modular and Open-Source Software Project for Quantum Simulations of Materials, *J. Phys.: Condens. Matter*, 2009, **21**, 395502.
39 J. P. Perdew, K. Burke and M. Ernzerhof, Generalized Gradient Approximation Made Simple, *Phys. Rev. Lett.*, 1996, **77**, 3865–3868.
40 D. K. Bhat and U. S. Shenoy, Zn: A Versatile Resonant Dopant for SnTe Thermoelectrics, *Materials Today Physics*, 2019, **11**, 100158.
41 D. K. Bhat and S. U. Shenoy, Resonance Levels in GeTe Thermoelectrics: Zinc as a New Multifaceted Dopant, *New J. Chem.*, 2020, **44**, 17664–17670.
42 H. C. Chen, C. W. Huang, J. C. Wu and S. T. Lin, Theoretical Investigation of the Metal-Doped $SrTiO_3$ Photocatalysts for Water Splitting, *J. Phys. Chem. C*, 2012, **116**, 7897–7903.
43 M. J. S. Mohamed and D. K. Bhat, A Facile Microwave Approach to Synthesize RGO-$BaWO_4$ Composites for High Performance Visible Light Induced Photocatalytic Degradation of Dyes, *AIMS Mater. Sci.*, 2017, **4**, 487–502.
44 M. Sethi, S. U. Shenoy and D. K. Bhat, Porous Graphene-$NiCo_2O_4$ Nanorod Hybrid Composite as High Performance Supercapacitor Electrode Material, *New J. Chem.*, 2020, **44**, 4033–4041.
45 I. C. Amaechi, A. Hadj Youssef, D. Rawach, J. P. Claverie, S. Sun and A. Ruediger, Ferroelectric Fe–Cr Codoped $BaTiO_3$ Nanoparticles for the Photocatalytic Oxidation of Azo Dyes, *ACS Appl. Nano Mater.*, 2019, **2**, 2890–2901.
46 M. Sethi, S. U. Shenoy and D. K. Bhat, Porous graphene - $NiFe_2O_4$ Nanocomposite with High Electrochemical Performance and High Cyclic Stability for Energy Storage Application, *Nanoscale Adv.*, 2020, **2**, 4229–4241.
47 M. Sethi, H. Bantawal, S. U. Shenoy and D. K. Bhat, Eco-friendly Synthesis of Porous Graphene and Its Utilization as High Performance Supercapacitor Electrode Material, *J. Alloys Compd.*, 2019, **799**, 256–266.
48 S. Kawasaki, K. Akagi, K. Nakatsuji, S. Yamamoto, I. Matsuda, Y. Harada, J. Yoshinobu, F. Komori, R. Takahashi, M. Lippmaa and C. Sakai, Elucidation of Rh-Induced In-Gap States of Rh: $SrTiO_3$ Visible-Light-Driven Photocatalyst by Soft X-ray Spectroscopy and First-Principles Calculations, *J. Phys. Chem. C*, 2012, **116**, 24445–24448.
49 M. M. J. Sadiq, U. S. Shenoy and D. K. Bhat, Novel RGO–$ZnWO_4$–Fe_3O_4 Nanocomposite as High Performance Visible Light Photocatalyst, *RSC Adv.*, 2016, **6**, 61821–61829.

